Nanoscale

Journal Name

ARTICLE

Improving organic tandem solar cells based on water-processed nanoparticles, by quantitative 3D nanoimaging

E. B. L. Pedersen,[a] D. Angmo,[a] H. F. Dam,[a] K. T. S. Thydén,[a] T. R. Andersen,[a] E. T. B. Skjønsfjell,[b] F. C. Krebs,[a] M. Holler,[c] A. Diaz,[c] M. Guizar-Sicairos,[c] D. W. Breiby[b] and J. W. Andreasen[a]

Organic solar cells have great potential for upscaling due to roll-to-roll processing and a low energy payback time, making them an attractive sustainable energy source for the future. Active layers coated from water-dispersible Landfester particles enable greater control of the layer formation and easier access to the printing industry, which has reduced the use of organic solvents since the 1980s. Through ptychographic X-ray computed tomography (PXCT) we image quantitatively a roll-to-roll coated photovoltaic tandem stack consisting of one bulk hetero junction active layer and one Landfester particle active layer. We extract the layered morphology with structural and density information including porosity present in the various layers and the silver electrode with high resolution in 3D. The Landfester particle layer is found to have an undesired morphology with negatively correlated top- and bottom interfaces, wide thickness distribution and only partial surface coverage causing electric short circuits through the layer. By top coating polymer material onto the Landfester nanoparticles we eliminate the structural defects of the layer such as porosity and roughness, and achieve the increased performance larger than 1V expected for a tandem cell. This study highlights that quantitative imaging of weakly scattering stacked layers of organic materials has become feasible by PXCT, as this information cannot be obtained by other methods. In the present study this technique specifically reveals the need to improve the coatability and layer formation of Landfester nanoparticles, thus allowing improved solar cells to be produced.

Introduction

In the pursuit of sustainable energy production only a few technologies have the potential to meet the world's energy demand and the one with the biggest potential is solar energy.[1] The most common photovoltaic technology is based on crystalline silicon, and is hampered by a long energy payback time between 1.7 and 2.7 years,[2] and therefore also by a high energy price. Organic photovoltaics is an emerging solar cell technology with a high upscaling potential and low energy payback time between 0.3 and 0.5 years[2] due to mass production methods of roll-to-roll coating of abundant elements.[3] It has been suggested that it will be possible to reach energy payback time of less than 1 day,[4] and large scale deployment of organic photovoltaic modules has already been demonstrated.[5]

Two of the challenges for consistent large scale production of multilayered organic electronics are solvents redissolving underlying layers and the control of molecular self-assembly within layers.[6] Packing surfactants around the organic molecules, thus

a. Department of Energy Conversion and Storage, Technical University of Denmark, Frederiksborgvej 399, 4000 Roskilde, Denmark
b. Department of Physics, Norwegian University of Science and Technology, Høgskoleringen 5, 7491 Trondheim, Norway
c. Paul Scherrer Institut, 5232 Villigen PSI, Switzerland
Electronic Supplementary Information (ESI) available: Determination of spatial resolution, simulations of partial volume effects, and comparison and explanation of threshold segmentation and Markov field segmentation. See DOI: 10.1039/x0xx00000x

turning them into water dispersible Landfester particles, offers an opportunity to both control the internal structure through the particle fabrication process[7] and to produce complex multilayer structures even with simultaneous coating of more than one layer at a time.[8] Furthermore, water based inks are non-toxic and ease large-scale production by removing the safety requirements associated with toxic and flammable organic solvents. Water based inks would also enable easier transition to large scale production by accessing the existing printing industry, which has made use of organic solvents since the 1980s,[9] and reduce the need to develop custom-built fabrication lines for organic photovoltaics.[10]

Water based inks are common for intermediate layers such as poly(3,4-ethylenedioxythiophene) polystyrene sulfonate (PEDOT:PSS) and ZnO, whereas water dispersible photoactive nanoparticles need further development to be applied widely. The major issue is that the power conversion efficiency is 1/3 compared to that achieved for bulk hetero junctions.[11] A recent improvement was made with surfactant free nanoparticles cast from alcohol based solvents with device power conversion efficiencies of 4%.[12] However, without particle stabilization such inks might be unstable and therefore difficult to upscale. The layer formation of active nanoparticles has mainly been studied by examining the surface properties using Atomic Force Microscopy (AFM) and the internal layer structure by using Transmission Electron Microscopy (TEM) or Scanning Transmission X-Ray Microscopy (STXM) on stand-alone nanoparticle layers.[11,13–15] To get a more complete image of the failure mechanisms it is desirable to image the full layer structure whilst embedded in a complete device stack, so that both the individual layers and the relevant interfaces can be examined.

Until recently, even though a multitude of techniques were applied to measure the morphology and structure of organic photovoltaic devices, none of them provided three-dimensional (3D) structural information of an entire device.[16] Ptychographic X-ray computed tomography (PXCT)[17] provides quantitative 3D images and has already been used to facilitate the development of an organic photovoltaic tandem device.[18] The technique is ideal for proving structural information for organic photovoltaics since it provides the nanometer resolution necessary to image thin layers in organic photovoltaics. PXCT at multi keV photon energies provides sufficient penetration power to image materials with thicknesses in the order of tens of microns, contrary to many high resolution X-ray and electron based techniques such as transmission electron microcopy and scanning transmission X-ray microscopy which are typically limited to about 100 nm thickness.[16] Experimentally PXCT has been demonstrated to reach 16 nm isotropic 3D resolution on a 6 micron thick for-purpose high-contrast object.[19]

Here we report 3D PXCT imaging of an organic photovoltaic tandem solar cell. The main purpose is to investigate layer formation of the Landfester nanoparticles as well as to investigate their influence on surrounding layers and interfaces in a tandem device, and the effect on solar cell performance. A tandem structure is purposefully employed for this study because it presents added complexity to the device structure as up to 10 layers are present with various metal, organic, and inorganic individual layers, and interfaces comprising a combination of these materials. Such a complex system covering phase separation from below 10 nm to tens of nm's allows probing the resolution limit of the employed PXCT imaging technique, for the materials in an actual working device. We demonstrate the mathematical tools to extract quantitative information about layers and interfaces from the PXCT tomogram. Furthermore, the tandem solar cells are realized by all solution-based, industrially relevant, ambient coating and printing techniques, thus adding application relevance to the results of this study. Additionally, we use a tandem structure with one of the active layers comprising a conventional bulk hetero-junction and the other consisting of Landfester nanoparticles. This allows the direct comparison of the two kinds of active layers within the same dataset, and at the same time provides the opportunity to investigate the material interfaces and layer structures in the complete device. The quantitative nature of ptychographic tomography also allows investigation of mass density variations by extracting electron densities and comparing them to expected values of the known materials.

Results and discussion

We investigate the nanostructure of the organic tandem cell presented in **figure 1** using a sub tomogram of the central region of the sample to exclude artifacts from material redisposition at the sample sides originating from the sample preparation. The layered stack of materials was produced by slot-die coating material solutions and nanoparticle dispersions on a flextrode substrate[20] using a lab scale roll-coater[21]. The structure showed photo electric performance and a pillar of solar cell was cut and mounted on a sample holder using focused ion beam (FIB) milling. Since the PXCT electron densities were measured relative to air, all electron densities in the tomogram were corrected with the electron density of air, 10^{-3} Å^{-3}. We have obtained a ptychographic tomogram of the tandem structure with a spatial resolution of 20 nm, as estimated by Fourier shell correlation[22] (see supporting information for

further details). Our prime target of investigation is the morphological differences between the active layer consisting of Landfester particles and the other active layer being a conventional bulk heterojunction based on PDTSBT-F:PCBM (see experimental for full name). The nearby PEDOT:PSS layers (used for charge transport) have little contrast to the active layers because both types of layers mainly consist of carbon. In our analysis, the photovoltaically active and PEDOT:PSS layers will therefore be analyzed as *one* layer referred to as organic layers: PDTSBT-F:PCBM and PEDOT:PSS as the organic bulk heterojunction layer, P3MHOCT:PCBM Landfester and PEDOT:PSS as the organic nanoparticle layer.

In the analysis of the tomogram, efforts were made to keep the physical significance of the segmentation by utilizing the electron density values and their spatial distribution with Markov field segmentation. The histograms of electron densities were fitted by two kinds of distributions: Gaussian peak shapes - corresponding to pure materials, and power functions with Gaussian cut-offs - corresponding to partial volumes i.e. interface voxels with more than one material present, see supporting information. This was done according to the shape of the electron density histogram and the prior knowledge of the distribution of layers within the solar cells. Nearest neighbor information was included in the segmentation by using a Markov field in order to accurately label materials with overlapping electron densities (see supporting information).

Nanoparticle and bulk heterojunction structure

The active Landfester nanoparticle layer is porous and contains small domains of air as seen in **figure 1**. From the electron densities it is apparent that the scale of the porosity is below the limit of 20 nm imposed by the resolution, since the electron densities arise from partial volume effects, i.e. voxels with both nanoparticles and air, and the air cannot originate from the sample surface since only an interior section of the sample is studied. The layers have been roll coated at 60°C and the final device was annealed at 100°C, so it is possible that further annealing before coating subsequent layers would remove or reduce porosity. The bulk heterojunction is homogeneous, as expected (see figure 1). The air between the nanoparticles reveals that the active layer only partially covers the surface. With only partial coverage the overlying PEDOT:PSS is most likely penetrating the active layer. The zinc oxide segment provides clear proof of a short circuit with instances of spikes penetrating the nanoparticle layer, as seen on figure 1D.

Short circuits through the nanoparticle layer are also evident from the electrical device characterization presented in **table 1**. The low open circuit voltage (V_{oc}) of the tandem device indicates a single junction device. It is comparable to the performance of single junction cells with only a bulk heterojunction layer, supporting the findings from ptychographic tomography of a non-functioning nanoparticle layer. The limited contact through the nanoparticle layer and the longer charge path also cause the short circuit current (J_{sc}) to decrease, compared to the single junction BHJ device. The failure of the device is therefore not primarily a result of poor photovoltaic performance of the nanoparticles, but a result of the nanoparticles only forming a partially covering layer. The decreased photoelectric performance of the nanoparticles due to the undesirable layer morphology highlights the need to consider the processing and layer formation of the nanoparticles as a key parameter to optimize in addition to optimization of the internal structure and photoelectric properties of the organic nanoparticles

Nanoscale Accepted Manuscript

themselves.[7] Such optimization could consist of employing different surfactants or even mixtures of cat- and anionic surfactants.[15]

Electron density

Apart from high spatial resolution, ptychographic tomography also provides accurate quantitative information about the spatially resolved electron density, $\rho_e(\mathbf{r})$, obtained from tomographic reconstruction of phase contrast projections.[23,24] For the tandem cell, we find three layers of particular interest due to their electron density distributions: The two zinc oxide layers, the silver electrode and the organic layer containing nanoparticles. Based on the segmentation a slice containing only these layers along with histograms of their electron density distributions is presented in **figure 2**.

The zinc oxide layers have a reduced electron density, consistent with the fact that these layers are processed from ZnO nanoparticles. The normal electron density for bulk zinc oxide is 1.60 Å^{-3}, whereas the mean observed electron density is 0.96 Å^{-3}. In the analysis of this reduced electron density we have already considered partial volume effects between zinc oxide and organic materials, which have been classified into its own category as shown in figure 2B. The remaining pure zinc oxide phases have a Gaussian density distribution as expected due to experimental uncertainties. The reduction in electron density of 60% compared to the bulk material is therefore a real physical property which most likely arises from the nanoparticles that form the zinc oxide layers. The particulate structure could result in looser material packing or even nanometer scale porosity below our resolution limit.

The silver electrode also consists of nanoparticles, and we observe porosity in the silver electrode as opposed to our previous experiments.[18] In those experiments PEDOT:PSS infiltrated the whole electrode, whereas in the current study it only infiltrates the first 50-100 nm of a 1 micron thick electrode. This might be explained by a thicker PEDOT:PSS layer used in the previous experiment, which left sufficient material to penetrate the electrode.

For the organic materials we see little difference between the materials P3MHOCT:PCBM and PEDOT:PSS. They both mainly consist of carbon and exhibit a single Gaussian peak of the electron density. The porosity previously observed in the nanoparticle layers constitutes partially filled volumes with organic material and air. A small amount of the observed voxels (917 of 3.9×10^6) has electron densities equal to or below those of air (10^{-3} Å^3). The reason why we can identify all of the partial volumes as sub-resolution porosity is that air is the only constituent expected in the sample with lower electron density than carbon. Air is evidently present due to the observation of voxels with electron densities lower or equal to air beyond what can be expected from the Gaussian electron density distributions from organic material i.e. 917 voxels have electron density less or equal to 10^{-3} Å^3 whereas 6×10^{-13} voxels would be expected from the observed Gaussian distribution of the organic material. Thus, it is plausible that all the low density voxels have partial volumes of organic material and air, since no air voxels should be present as we are only looking at the interior of the sample.

Interfaces

Interfaces are particularly important in organic photovoltaics because they are critical for charge transport and successful device performance. PXCT provides nanometer scale information of the interfaces and as opposed to other methods, e.g. AFM, it can be used to investigate correlations between subsequent layers. A detailed quantitative analysis of the tandem interfaces and layers is presented in **figure 3**. The top-bottom correlation indicates how much a given layer is affected by the topology of the underlying layer. The 1 micron thick silver layer has low top-bottom interface correlation, likely due to the coarse structure caused by the nanoparticles in the layer. However, the resulting top surface roughness remains low. The observed characteristics of the silver electrode and subsequent PEDOT:PSS layer might also be due to the printing methods; the silver was flexographically printed and the PEDOT:PSS was rotary-screen printed.[20] Previously large scale variations have been found in the thickness of similar silver electrodes[25], but this and a previous ptychography experiment[18] find a rather flat silver layer. It might be explained by the subsequent rotary-screen printing altering the silver interface thus ensuring a more planar layer with low roughness. The remaining layers, with the exception of the organic area with nanoparticles, have a high degree of positive interface correlations and mostly narrow thickness distribution.

The organic layer with active nanoparticles has a negative interface correlation in addition to a high surface roughness of the top interface and a wide size distribution. Negative top-bottom interface correlation is undesirable since it results in a wide thickness distribution (thick and thin regions), and increases the risk of short circuits. A wide thickness distribution is undesirable for large-scale production because the optimal material thickness cannot be deployed and results in reduced photoelectric performance. The roughness of the organic nanoparticle layers also increases to three times the roughness of the underlying zinc oxide layer and is only gradually reduced in the subsequent layers.

The organic nanoparticle layer distinguishes itself by having overall characteristics that negatively affect the other layers, e.g. the tail in the size distribution of the top zinc oxide layer is caused by spikes through the active nanoparticles. Since the main difference between the two active layers is the structure (bulk versus nanoparticles), the undesired behavior of the active nanoparticle layer could easily be attributed solely to the layer consisting of nanoparticles. However, the remaining layers are all cast from particles that show good layer characteristics, including the inorganic zinc oxide nanoparticles, the organic PEDOT:PSS gel particles and the large silver particles. The surface energies and particle interactions appear to be undesirable only for the active layer nanoparticles.

The negative top-bottom interface correlation could suggest that the Landfester nanoparticles in the active layer initially locate themselves in topological minima and afterwards aggregate to form thick layers around these positions. The difficulties of proper nanoparticle layer formation have also been documented previously, where multiple castings have been necessary to produce sufficient layer thickness.[14] One of the main differences between the Landfester particles and the other materials is the charged surfactant necessary for proper particle stabilization in water. To increase the coatability of the nanoparticles a polar substrate or substrate modification could be applied, however it would both need to be water insoluble and to conserve the photovoltaic

performance of the device. Another option is to reduce the net particle charge by applying a nonionic surfactant. Surfactant-free particles have also been dispersed in ethanol,[12,13] but without ionic surfaces, steric stabilization will likely be needed for long term ink stability.

Overcoming structural defects in the nanoparticle layer

The main structural fault of the roll coated nanoparticle layer was found to be the shorts circuits through the layer as a result of voids between the nanoparticles and its high surface roughness. It is thus critical to demonstrate that an improved nanoparticle layer will reach the performance expected of a tandem solar cell, as we have done in a follow-up experiment. By coating active layer materials on top of the nanoparticle layers, the voids can be filled up with material with lower conductivity than PEDOT:PSS, and ZnO and electric short circuits through the layer can be prevented. By partially redissolving the nanoparticle layer and filling up the rough areas with new material, one will of course reduce the roughness of the layer (and subsequent layers). A schematic overview of the electric performance in a tandem structure and the visual appearance of smoothened layers are shown in **figure 4**. From the photograph it is clear that only minor redissolving of the nanoparticle layer takes place as the nanoparticle layer's edges and structures are visible through the P3MHOCT layer on top. As regards the photovoltaic performance, clear tandem behavior can be seen by a V_{oc} higher than the single BHJ (0.6V). Only devices with top coated P3MHOCT reach those voltages with a V_{OC} of 0.96 V using front illumination, whereas double sided illumination[25] gives 1.06 V). It is not surprising that devices with top coated P3MHOCT have higher potential than devices with top coated PCBM, because P3MHOCT is a hole conductor and better matches the energy levels of the device structure. The devices were characterized with front illumination in which photons first pass through the nanoparticle active layer (**table 2**), and double sided illumination, as described by Andersen et al,[25] with photons incident from both sides with the use of mirrors (**table S1**). The greatest difference between the two illumination forms is found for pure NP devices. For these devices photo absorption in the NP layer will not contribute to the device performance due to the shorts through the NP layer. We also see that the V_{OC} does not change, and it should be noted that more than 50% of all devices had resistor behavior after switching. The experiments show that if coated nanoparticles films can achieve the same layer characteristics regarding porosity and roughness as solution cast active layers, they can form successful active layers in tandem devices. Future experiments should focus on optimizing the layer formation by choice of surfactant, polar surface modifications, intermediate heating steps and other means suitable for large-scale production.

Remarks on solar cell performance

In this paper, our primary motivation is to investigate the feasibility of a Landfester particle layer in a tandem structure, its layer formation and its impact on surrounding materials and interfaces and therefore on the functionality of the solar cell. V_{oc} is chosen to be the primary indicator of a functional tandem solar cell as other photovoltaic parameters are dependent on optimization of the solar cell. Optimization was not carried out because it would have been an unfruitful pursuit owing to several limitations of the device architecture that is yet to be solved but is beyond the scope of this study.

The nanoparticle polymer P3MHOCT is a thermocleavable polymer which, albeit inherently exhibiting lower PCE, is attractive for its

significantly higher stability compared to other photoactive polymers. Thermocleaving allows this polymer to attain higher efficiency and stability[36]. However, in the current tandem structure, thermocleaving could not be pursued. The PET substrate employed in the roll-coated tandem devices here cannot sustain higher than 140 ^{o}C whereas thermocleaving of P3MHOCT requires temperature above 220 ^{o}C.[35] Furthermore, the nanoparticle approach generally tends to result in lower J_{sc} and FF attributed to inhomogeneity in the layer thickness[37] (surface coverage) of the nanoparticle layer (as this study has now quantified (Figure 2)), and the presence of residual surfactant bonded to the surface of the nanoparticles, as well as the size of the nanoparticles. These limitations are envisioned surmountable through various routes,[12,38,39] although beyond the scope of this study. Using the current processing approach, we have shown the nature of all the layers and their interplay in the surrounding layers, particularly the challenges presented by the Landfester nanoparticle layer.

In Figure 4B, the V_{oc} of a tandem cell based on a front sub-cell with P3MHOCT:PCBM nanoparticle layer and the rear cell based on a bulk heterojunction PDTSBT-F:PCBM layer results in a V_{oc} which is less than either of the individual sub-cells (0.6 -6.5 V). This clearly demonstrates that the Landfester particle layer, despite its very high thickness (~900 nm), causes short circuits in not only the front sub-cell but also in the back cell, in agreement with the negative top-bottom correlation found at the interfaces of the nanoparticle layer and its impact on the subsequent layers and interfaces (see section on *Interfaces*). Passivating this interface with the introduction of a PCBM layer (100-200 nm) clearly mitigates this device failure as V_{oc} is significantly improved although not to the point of full recovery of an ideal tandem cell. Only upon coating of a P3MHOCT:PCBM bulk heterojunction layer on top of the nanoparticle layer, the V_{oc} approaches proper tandem device characteristics. Because of the lack of current matching in the device, the V_{oc} of the tandem does not equal the sum of the individual junctions. This is also attributed to the use of a flexible substrate that generally results in lower V_{oc} than on rigid substrates as glass.[40] The use of three distinct layers of PEDOT at all electrical contact points (cathode, anode, and the intermediate layer) generally also results in lower V_{oc} due to the low in-built field across the sub-cells.

Conclusions

Using ptychographic X-ray computed tomography (PXCT), we have investigated an organic tandem solar cell with two active layers: one consisting of a bulk heterojunction and one of Landfester nanoparticles. We have found that the primary failure mechanism of the device is short circuits connecting PEDOT:PSS and zinc oxide layers through the active Landfester nanoparticle layer. This is also evident in the photovoltaic performance where the open circuit voltage, V_{OC}, is similar to the single junction device consisting of a bulk heterojunction material only, and the short circuit current, J_{sc}, is reduced below the single junction device level.

The electron densities extracted from the PXCT reveal that layers cast from zinc oxide nanoparticles only have 60% of the expected density for the bulk materials, indicating a porous layer or less dense material packing due to the nanoparticle structure. The silver electrode is porous with large air cavities. Similarly, the organic layer containing active nanoparticles has sub-resolution porosity i.e. below 20 nm. A thorough and state-of-the-art interface analysis shows how all layers with the exception of the active nanoparticle layer have a positive top-bottom interface correlation. The active

nanoparticle layer on the other hand has negatively correlated top- and bottom interfaces, which also implies a wide distribution in layer thickness and a high interface roughness. The surface roughness is gradually reduced in subsequent layers and it never decreases to the levels observed below the nanoparticle active layer. To make nanoparticle active layers a viable alternative to bulk heterojunctions, the coatability of the active nanoparticles will need to be improved. By top coating P3MHOCT on the nanoparticle layer we demonstrate that tandem potentials above 1V can be achieved when the nanoparticle layers structural flaws i.e. porosity and roughness, are reduced. We conjecture that the structure of the nanoparticle layer can be improved either through polar surface modifications, heating steps or by reduction of the net charge on the particles, for instance by use of nonionic surfactants. The otherwise unobtainable tomographic information makes PXCT a critical tool to face the nano-engineering challenges one must overcome to realize organic photovoltaics as a technology.

Experimental

Full chemical names
Ag = Silver, PEDOT:PSS = poly(3,4-ethylenedioxythiophene):polystyrene sulfonate, ZnO = zinc oxide, PET = polyethylene terephthalate, Active - Bulk heterojunction = PDTSBT-F:PCBM, PDTSBT-F = poly[(4,4'-bis(2-ethylhexyl)dithieno[3,2-b:2',3'-d]silole)-2,6-diyl-alt-4,7-(5-fluoro-2,1,3-benzothiadiazole)] (previously reported as P2[18]), PCBM = phenyl-C61-butyric acid methyl ester, Active – nanoparticles = 1:1 P3MHOCT:PCBM Landfester particles, P3MHOCT = poly-(3-(2-methylhexyloxycarbonyl)dithiophene), Organic BHJ = PDTSBT-F:PCBM + PEDOT:PSS , Organic NP = P3MHOCT:PCBM Landfester particles + PEDOT:PSS.

Water dispersible Landfester nanoparticles
P3MHOCT and PCBM were mixed in a ratio of 1:1 in chloroform and processed into nanoparticles using the Landfester method[26] with Sodium Dodecyl Sulfate (SDS) as surfactant. The ink concentration was increased to 60 mg/mL by centrifugation.

Device fabrication
The device was made on a flextrode substrate which comprises PET/Ag grid/PEDOT:PSS produced by roll-to-roll printing and coating methods and is mass produced.[20] The remaining layers were fabricated by slot-die coating and flexographic printing on a lab scale roll-coater[21] as previously described[18] with the exception of the active nanoparticle layer. The Landfester nanoparticles, replacing the high band gap polymer used in reference[18], were coated at 60°C with a speed of 1.3 m/min and a flow rate of 0.220 mL/min resulting in a wet-layer thickness of 17 μm and an estimated dry layer thickness of 920 nm. The high layer thickness was found to be important to achieve a macroscopically uniform film during coating. The flextrode substrate used here differed from the one previously described[18] by having a thinner PEDOT:PSS layer. For coating PCBM or P3MHOCT on top of nanoparticles a 20 g/L chloroform solution was coated at 60°C with a speed of 1.0 m/min and a flow rate of 0.13 mL / min, thus resulting in a wet-layer thickness of 9 um and a dry layer thickness of 247 nm Complete details on materials, device preparation, and characterization is given in the supporting information.

Sample preparation
A 6.2 micron × 5.5 micron prism of solar cell was cut with a focused ion beam (FIB) in an area with bottom electrode but without top electrode. The sample was protected by a sputtered gold layer, and a deposited platinum layer prior to FIB cutting. A wolfram tip was fastened to the sample by platinum deposition and used to move the solar cell prism onto the sample holder, where it was welded in place by platinum deposition.

Ptychographic X-ray tomography
The sample was imaged using ptychographic X-ray tomography at the cSAXS beamline at the Swiss Light Source, Paul Scherrer Institut in Villigen, Switzerland, using the setup described in reference.[19] A coherent beam with 6.2 keV photon energy was focused by a Fresnel zone plate (FZP) of 170 micron diameter made of Au structures of 1.2 micron height and with an outer-most zone width of 60 nm, having a focal distance of about 51 mm at this energy. A central stop of 40 micron diameter and a sorting order aperture of 30 micron diameter were used to block diffraction orders from the FZP not contributing to the focus. The total flux provided by the FZP illumination is estimated to be about $3.6 \cdot 10^8$ photons/s. The sample was placed at a distance of about 1 mm downstream of the focus, in such a way that the beam had a diameter of about 3.3 micron at the sample position. A flow of nitrogen protected the sample from oxygen to reduce beam damage during the experiment. Ptychographic scans covering an area of 10×5 micron^2 (horizontal × vertical) were performed on a grid of concentric circles with a radial step size of 0.8 micron. Coherent diffraction patterns were recorded with an exposure time of 0.1 s at each position of the scan with a Pilatus 2M detector[27] placed 7.389 m downstream the sample. Ptychographic scans were repeated at 470 angular positions of the sample with respect to the beam, covering a total range of 180°. To adequately constraint the reconstruction in the areas where no data is measured due to intermodule gaps, we acquired angular projections at alternating detector positions[19] and reconstructions of two consecutive scans were carried out jointly, enforcing the illumination probe to be the same, using the algorithm in reference,[28] with 200 iterations of an algorithm based on the difference map[29] followed by 100 iterations of maximum likelihood refinement.[30] For ptychographic reconstructions a region of 600×600 pixels centered around the diffraction intensity distributions on the detector was selected, yielding reconstructed images with a pixel size of 14.3 nm. The reconstructed phase images from all projections were used for tomographic reconstruction after post-processing and registration according to the procedure described in reference.[31] For registration in the horizontal direction we further used a method based on tomography.[32] The resolution of the 3D dataset was estimated to be about 20 nm by Fourier shell correlation as detailed in the supporting information.

To estimate the dose, d, imparted on the specimen we use the expression $d = \mu N_0 \varepsilon / \rho$,[33] where μ is the linear attenuation coefficient of the specimen, N_0 is the number of incident photons per unit area, ε is the photon energy and ρ is the mass density of the specimen. With N_0 about 3.7×10^7 photons/μm^2 in our ptychographic scans and 470 projections, we estimate a dose of about 8.0×10^7 Gy on the PEDOT:PSS material, and 7.1×10^8 Gy in the Ag. We note that here we estimate the surface dose which in this sample overestimates the dose of Ag due to its thickness being about three times the attenuation length.

Data segmentation
The data was divided into subsets to ease segmentation. For each subset the voxel electron density distributions were fitted with

Gaussians for pure materials and power functions for material mixtures (see supporting information). Due to overlapping data fits a Markov field with alpha-expansion was used to enhance segmentation. A graph-cut algorithm was used to minimize the energy of the Markov field.[34] The weights of the nearest neighbors were fitted on actual data to match the relative voxel distribution of the fits for all densities simultaneously using a 2-norm (see also supporting information).

Acknowledgements

References

1. R. Perez and M. Perez, *IEA SHC Sol. Updat.*, 2009, **50**, 2.

2. S. Lizin, S. Van Passel, E. De Schepper, W. Maes, L. Lutsen, J. Manca, and D. Vanderzande, *Energy Environ. Sci.*, 2013, **6**, 3136.

3. F. C. Krebs, *Sol. Energy Mater. Sol. Cells*, 2009, **93**, 394–412.

4. N. Espinosa, M. Hösel, D. Angmo, and F. C. Krebs, *Energy Environ. Sci.*, 2012, **5**, 5117.

5. F. C. Krebs, N. Espinosa, M. Hösel, R. R. Søndergaard, and M. Jørgensen, *Adv. Mater.*, 2014, **26**, 29–39.

6. C. Newby, J.-K. Lee, and C. K. Ober, *Macromol. Res.*, 2013, **21**, 248–256.

7. J. J. Richards, C. L. Whittle, G. Shao, and L. D. Pozzo, *ACS Nano*, 2014, **8**, 4313–4324.

8. T. T. Larsen-Olsen, B. Andreasen, T. R. Andersen, A. P. L. Böttiger, E. Bundgaard, K. Norrman, J. W. Andreasen, M. Jørgensen, and F. C. Krebs, *Sol. Energy Mater. Sol. Cells*, 2012, **97**, 22–27.

9. K. Svendsen and K. S. Rognes, *Ann. Occup. Hyg.*, 2000, **44**, 119–124.

10. J. E. Carlé and F. C. Krebs, *Sol. Energy Mater. Sol. Cells*, 2013, **119**, 309–310.

11. S. Ulum, N. Holmes, D. Darwis, K. Burke, A. L. D. Kilcoyne, X. Zhou, W. Belcher, and P. Dastoor, *Sol. Energy Mater. Sol. Cells*, 2013, **110**, 43–48.

12. S. Gärtner, M. Christmann, S. Sankaran, H. Röhm, E.-M. Prinz, F. Penth, A. Pütz, A. E. Türeli, B. Penth, B. Baumstümmler, and A. Colsmann, *Adv. Mater.*, 2014, **26**, 6653–6657.

13. D. Darwis, D. Elkington, E. Sesa, N. Cooling, G. Bryant, X. Zhou, W. Belcher, and P. Dastoor, in *AIP Conf. Proc.*, 2011, vol. 1415, pp. 120–123.

14. A. Stapleton, B. Vaughan, B. Xue, E. Sesa, K. Burke, X. Zhou, G. Bryant, O. Werzer, A. Nelson, A. L. David Kilcoyne, L. Thomsen, E. Wanless, W. Belcher, and P. Dastoor, *Sol. Energy Mater. Sol. Cells*, 2012, **102**, 114–124.

15. S. Satapathi, H. S. Gill, L. Li, L. Samuelson, J. Kumar, and R. Mosurkal, *Appl. Surf. Sci.*, 2014, **323**, 13–18.

16. W. Chen, P. Nikiforov, and S. B. Darling, *Energy Environ. Sci.*, 2012, 8045–8074.

17. M. Dierolf, A. Menzel, P. Thibault, P. Schneider, C. M. Kewish, R. Wepf, O. Bunk, and F. Pfeiffer, *Nature*, 2010, **467**, 436–9.

18. H. F. Dam, T. R. Andersen, E. B. L. Pedersen, K. T. S. Thydén, M. Helgesen, J. E. Carlé, P. S. Jørgensen, J. Reinhardt, R. R. Søndergaard, M. Jørgensen, E. Bundgaard, F. C. Krebs, and J. W. Andreasen, *Adv. Energy Mater.*, 2014.

19. M. Holler, A. Diaz, M. Guizar-Sicairos, P. Karvinen, E. Färm, E. Härkönen, M. Ritala, A. Menzel, J. Raabe, and O. Bunk, *Sci. Rep.*, 2014, **4**, 3857.

20. M. Hösel, R. R. Søndergaard, M. Jørgensen, and F. C. Krebs, *Energy Technol.*, 2013, **1**, 102–107.

21. H. F. Dam and F. C. Krebs, *Sol. Energy Mater. Sol. Cells*, 2012, **97**, 191–196.

22. M. Van Heel and M. Schatz, *J. Struct. Biol.*, 2005, **151**, 250–262.

23. A. Diaz, P. Trtik, M. Guizar-Sicairos, A. Menzel, P. Thibault, and O. Bunk, *Phys. Rev. B*, 2012, **85**, 1–4.

24. M. Esmaeili, J. B. Fløystad, A. Diaz, K. Høydalsvik, M. Guizar-Sicairos, J. W. Andreasen, and D. W. Breiby, *Macromolecules*, 2013, **46**, 434–439.

25. T. R. Andersen, H. F. Dam, B. Andreasen, M. Hösel, M. V. Madsen, S. A. Gevorgyan, R. R. Søndergaard, M. Jørgensen, and F. C. Krebs, *Sol. Energy Mater. Sol. Cells*, 2014, **120**, 735–743.

26.   T. Kietzke, D. Neher, M. Kumke, R. Montenegro, K. Landfester, and U. Scherf, *Macromolecules*, 2004, **37**, 4882–4890.

27.   P. Kraft, a. Bergamaschi, C. Bronnimann, R. Dinapoli, E. F. Eikenberry, H. Graafsma, B. Henrich, I. Johnson, M. Kobas, a. Mozzanica, C. M. Schleputz, and B. Schmitt, *IEEE Trans. Nucl. Sci.*, 2009, **56**, 758–764.

28.   M. Guizar-Sicairos, I. Johnson, A. Diaz, M. Holler, P. Karvinen, H.-C. Stadler, R. Dinapoli, O. Bunk, and A. Menzel, *Opt. Express*, 2014, **22**, 14859.

29.   P. Thibault, M. Dierolf, O. Bunk, A. Menzel, and F. Pfeiffer, *Ultramicroscopy*, 2009, **109**, 338–43.

30.   P. Thibault and M. Guizar-Sicairos, *New J. Phys.*, 2012, **14**.

31.   M. Guizar-Sicairos, A. Diaz, M. Holler, M. S. Lucas, A. Menzel, R. a Wepf, and O. Bunk, *Opt. Express*, 2011, **19**, 21345–57.

32.   M. Guizar-Sicairos, J. J. Boon, K. Mader, A. Diaz, A. Menzel, and O. Bunk, *Optica*, 2015, **2**, 259–266.

33.   M. R. Howells, T. Beetz, H. N. Chapman, C. Cui, J. M. Holton, C. J. Jacobsen, J. Kirz, E. Lima, S. Marchesini, H. Miao, D. Sayre, D. a. Shapiro, J. C. H. Spence, and D. Starodub, *J. Electron Spectros. Relat. Phenomena*, 2009, **170**, 4–12.

34.   Y. Boykov and V. Kolmogorov, *IEEE Trans. Pattern Anal. Mach. Intell.*, 2004, **26**, 1124–37.

35.   T. Tromholt, S. A. Gevorgyan, M. Jørgensen, F. C. Krebs, and K. O. Sylvester-Hvid, *ACS Appl. Mater. Interfaces*, 2009, **1**, 2768–2777.

36.   M. Bjerring, J. S. Nielsen, A. Siu, N. C. Nielsen, F.C. Krebs, *Solar Energy Materials and Solar Cells* 92.7 (2008): 772-784.

37.   T. R. Andersen, T. T. Larsen-Olsen, B. Andreasen, A. P. Bottiger, J. E. Carle, M. Helgesen, E. Bundgaard, K. Norrman, J. W. Andreasen, M. Jørgensen, *ACS nano*. 2011, 5(5), 4188-4196.

38.   M. Helgesen, J. E. Carlé, B. Andreasen, M. Hösel, K. Norrman, R. Søndergaard, F. C. Krebs, *Polymer Chemistry.* 2012, 3(9), 2649-2655.

39   Y. Nan, X. Hu, T. T. Larsen-Olsen, B. Andreasen, T. Tromholt, J. W. Andreasen, D. M. Tanenbaum, H. Chen, F. C. Krebs, *Nanotechnology.* 2011, 22(47), 475301.

40   N. Li, D. Baran, G. D. Spyropoulos, H. Zhang, S. Berny, M. Turbiez, T. Ameri, F. C. Krebs, C. J. Brabec, *Advanced Energy Materials*. 2014, 4(11).
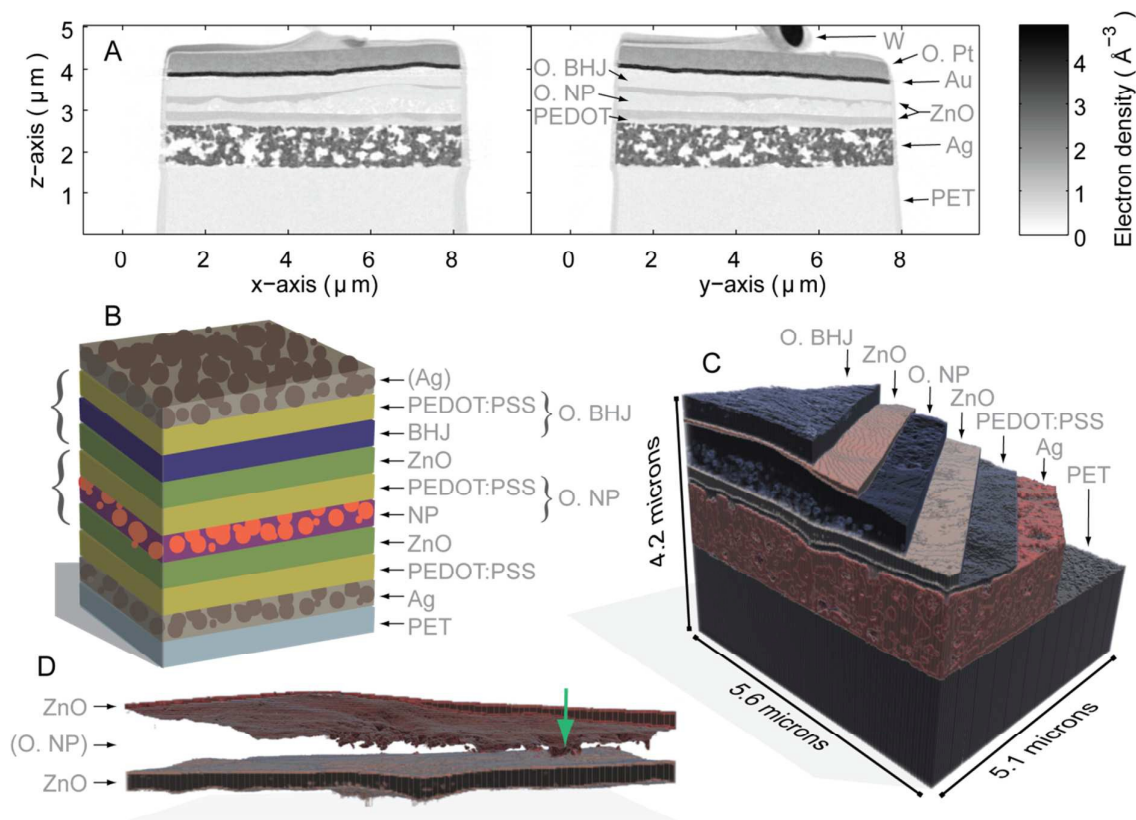
Journal Name

ARTICLE

Figure 1. Ptychographic X-ray computed tomography of an organic tandem solar cell A) Tomogram slices showing the electron density of the layers that make up the tandem solar cell. The top consist of tungsten (W), platinum rich organic molecules (O. Pt) and gold (Au) all originating from the sample preparation, and therefore not part of the photovoltaic device. The device itself consists of PEDOT:PSS and a bulk hetero junction (O. BHJ), zinc oxide (ZnO), PEDOT:PSS and Landfester nanoparticles (O. NP), PEDOT:PSS (PEDOT) and silver nanoparticles (Ag) on PET foil (PET). B) Schematic drawing of device layers (for full names see materials and methods). There are two active layers: A bulk hetero junction (BHJ) cast from organic solvent and a Landfester nanoparticle layer (NP) cast from water. The sample was cut from an area without top silver electrode, which therefore is not present in the tomogram. C) Cutaway view of segmented layers annotated as in B. The active layer consisting of nanoparticles contains sub 20 nm pores whereas the bulk heterojunction is homogeneous. D) Zinc oxide layers surrounding the nanoparticle layers. The vertical arrow marks a short circuit that penetrates through the porous nanoparticle layer.
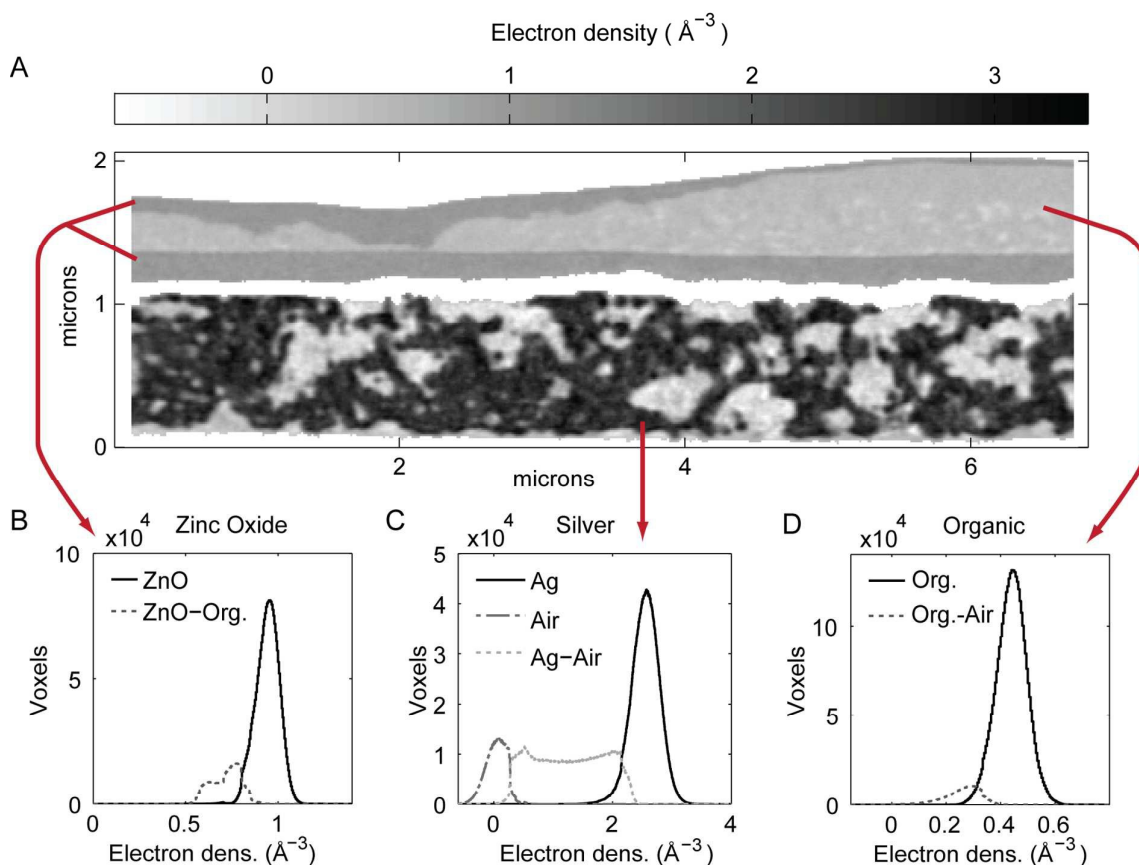
Figure 2. Electron density in the silver electrode and near the active layer consisting of nanoparticles. In A) we see a central tomography slice, near the short circuit of the nanoparticle layer only showing electron density for selected layers. The three histograms show electron density distribution based on segmentation. In B) we show the histogram of the two zinc oxide (ZnO) layers with a primary electron density of 0.96 Å^{-3} and partial volumes with nearby organic areas (ZnO-Org.). The electron density of the ZnO is only 60% of the expected bulk ZnO value (1.6 Å^{-3}), likely due to the ZnO layers being cast from nanoparticles. In C) we show the histogram of the silver layer, were silver (Ag), air and partial volumes with Ag-air mixture are distinguished. In D) we show the histogram corresponding to the organic layer, finding organic material (Org. = organic active nanoparticle and PEDOT:PSS) and sub-resolution porosity with nanoparticle materials and air (Org.-Air).
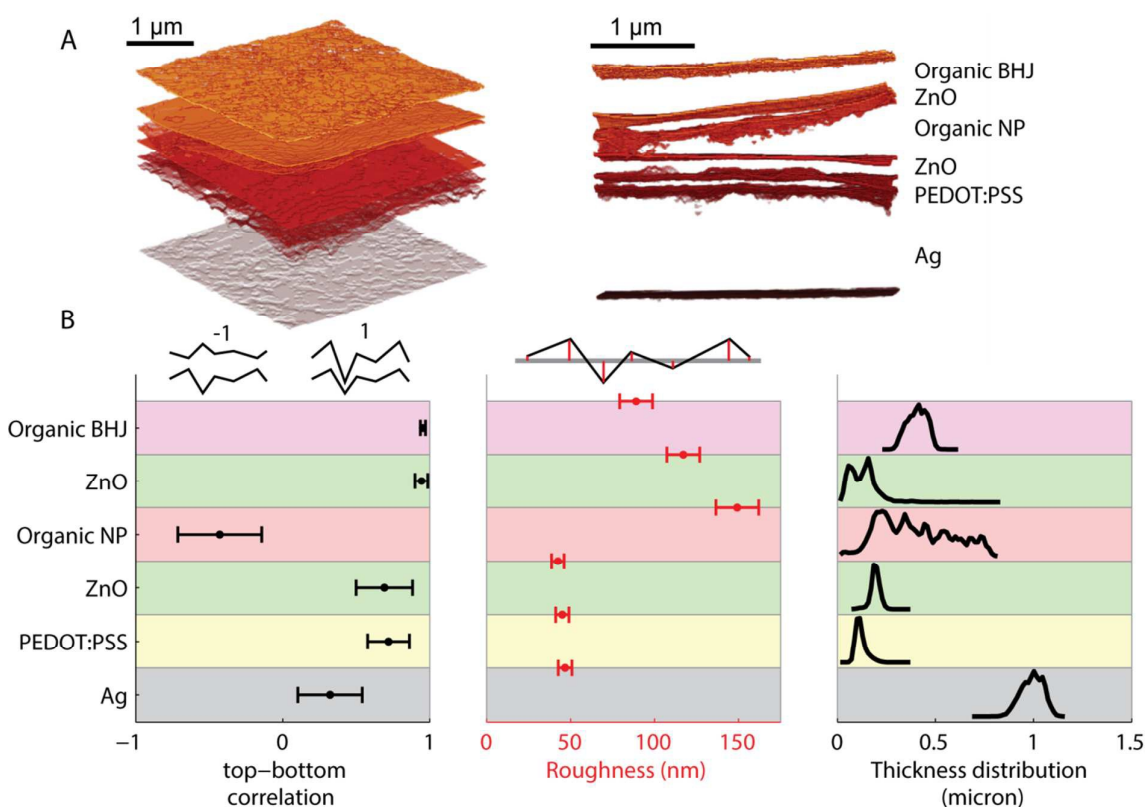
Figure 3. Interface analysis. A) Graphical representation of a part of the interfaces shown with top and side view with 1 micron scale bars. For full material names see materials and methods. B) Interface analysis of the different layers, from left to right: Correlation between the interface below and above the layer, roughness of interfaces and thickness distribution of the layers. The schematics above the graphs indicate the measured property i.e. top-bottom correlation is -1 for surfaces with opposite structure and 1 for identical structure disregarding scaling whereas roughness is defined as the average distance to a completely plane layer (red lines). The tail of the top ZnO thickness distribution is likely from spikes going through the organic NP layer.
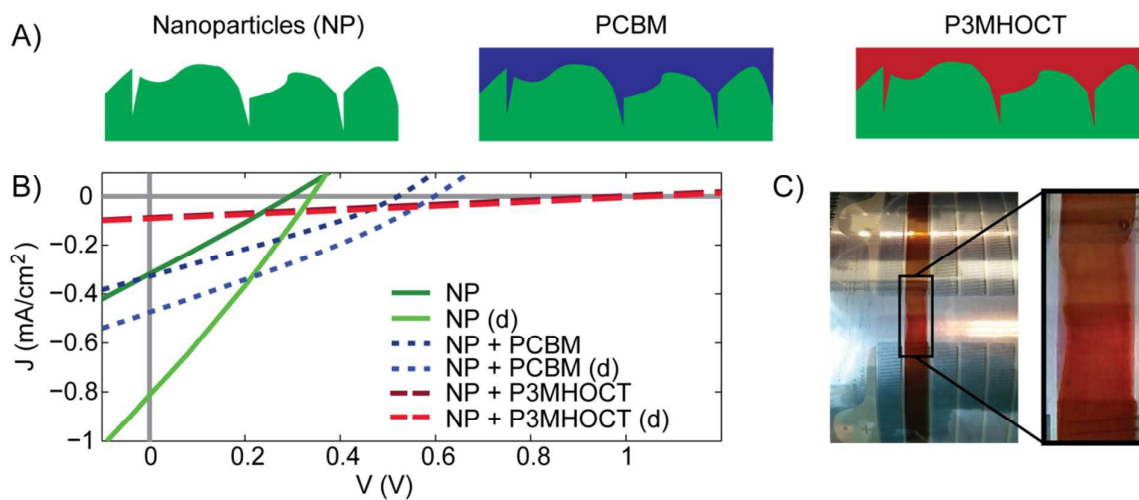
Figure 4. Measured tandem performance with alternative organic NP layers A) Schematics, from the left: Only nanoparticles, nanoparticles with solution cast PCBM on top, nanoparticles with solution cast P3MHOCT on top. B) The corresponding IV-curves for front illuminated devices, or double sided illuminated devices marked by (d). Devices with top coated P3MHOCT show clear tandem voltage (> 1V) C) Photograph of coating of P3MHOCT on NPs. The NP layer remains visible below the P3MHOCT. It is clearest outside the zinc oxide areas where the NPs are dewetting more than P3MHOCT cast from solution.

Table 1. Device performance is shown for the studied tandem structure with both an active layer of nanoparticles (NP) and a bulk hetero junction (BHJ), and is further compared to a previously measured and published data.[18,35] BHJ_1 = PDTSBT-F:PCBM, BHJ_2 = P1:PCBM (P1 is a high bandgap polymer described in reference.[18]), BHJ_3 = P3MHOCT:PCBM and NP_3 = P3MHOCT:PCBM as Landfester particles. The structure in our experiment is similar to the previous successful tandem structure[18] except having P3MHOCT:PCBM nanoparticles instead of a high band gap BHJ. The low V_{oc} of our tandem device with an NP layer indicates it only functions as a single junction device, since the V_{oc} otherwise should exceed the V_{oc} of the single junction and approach the combined V_{oc} of the two single junctions of 1.2 V.

	V_{oc}	J_{sc}	FF	PCE
	(V)	(mA cm^{-2})	(%)	(%)
Tandem $BHJ_1 - NP_3$	0.52	0.67	35.7	0.12
Tandem[18] $BHJ_1 - BHJ_2$	1.32	4.3	46.9	2.67
Single[18] BHJ_1	0.61	4.98	45.2	1.37
Single[35] BHJ_3	0.65	4.09	33.6	0.90

Table 2. Device performance is shown for the studied tandem structure comprising both an active layer of nanoparticles (NP) and a bulk hetero junction (BHJ) compared with devices where an additional layer is mitigating short circuits. Corresponding single devices are also shown. BHJ_1 = PDTSBT-F:PCBM, BHJ_3 = P3MHOCT:PCBM and NP_3 = P3MHOCT:PCBM as Landfester particles. Both single and tandem devices are built on Flextrode and uses similar materials and processing conditions. All devices here are not encapsulated and therefore vary from values reported in Table 1 for similar devices. The device performances with double sided illumination are given in Table S1 in the supporting information.

	V_{oc}	J_{sc}	FF	PCE
	(V)	(mA cm^{-2})	(%)	(%)
Tandem $BHJ_1 - NP_3$	0.29	0.45	25.86	0.03
Tandem $BHJ_1 - NP_3$+ PCBM	0.52	0.47	28.07	0.12
Tandem $BHJ_1 - NP_3$+ BHJ_3	0.96	0.12	24.57	0.03
Single BHJ_1[1]	0.57	3.25	30	0.56
Single NP_3	0.09	0.05	24.40	0.00
Single NP_3+PCBM	0.01	0.16	24.39	0.00

Nanoscale Accepted Manuscript

Ptychographic tomography provides 20 nm 3D resolution of a roll-to-roll coated organic tandem solar cell containing active layer cast from water-dispersible Landfester nanoparticles**.** Porosity is found in the silver electrode and active layer cast from nanoparticles. Interface characterization indicates structural defects in the nanoparticle layer such as roughness and shorts through the layer. When the defects are overcome by top coating polymer material, tandem performance with more than 1V is achieved. This highlights the need to improve intrinsic coatability of water dispersible nanoparticles to make them a viable alternative to bulk heterojunctions.

Keyword: tandem solar cells; multilayer materials; flexible materials; ptychography; organic nanoparticles

Emil B. L. Pedersen, Dechan Angmo, Henrik F. Dam, Karl T. S. Thydén, Thomas R. Andersen, Eirik T. B. Skjønsfjell, Frederik C. Krebs, Mirko Holler, Ana Diaz, Manuel Guizar-Sicairos, Dag W. Breiby and Jens W. Andreasen*

ToC figure
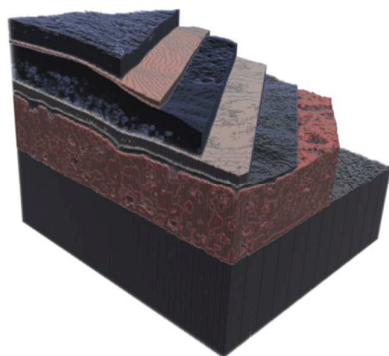
Supporting Information

Water-processed organic tandem solar cells improved by quantitative 3D nanoimaging

Emil B. L. Pedersen, Dechan Angmo, Henrik F. Dam, Karl T. S. Thydén, Thomas R. Andersen, Eirik T. B. Skjønsfjell, Frederik C. Krebs, Mirko Holler, Ana Diaz, Manuel Guizar-Sicairos, Dag W. Breiby and Jens W. Andreasen*

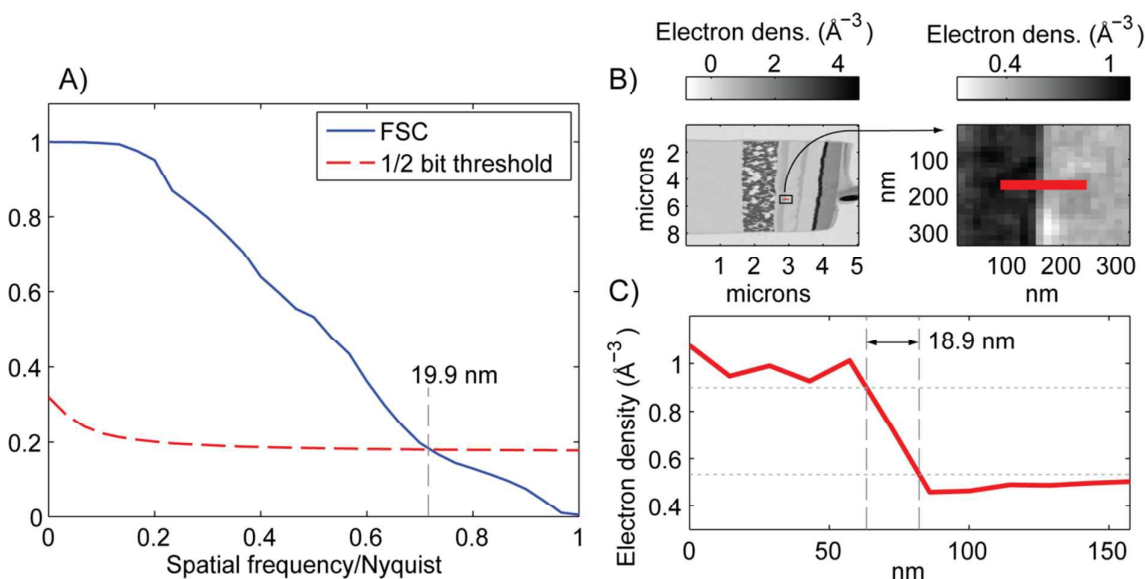**S.1. Spatial resolution by Fourier shell correlation**

Figure S1: A) Fourier shell correlation (FSC) calculated for a central part of the tomographic data shown in the in main article.
The 0.5 bit threshold intersects at 0.72 spatial frequency / Nyquist limit which with a Nyquist limit of 14.3 nm corresponding to 14.3 nm / 0.72 = 19.9 nm isotropic half period spatial resolution. B) Schematics of line scan shown in C) which yield 18.9 nm spatial resolution with the 10%-90% criterion.

The sample was measured at 470 projections that were reconstructed to a voxel side length at a half-period Nyquist limit of 14.3 nm. The resolution of the 3D dataset obtained by ptychographic tomography was estimated by Fourier shell correlation (FSC),[19,22] using two tomograms each computed from half of the projections. In Figure S1 we show in blue the computed FSC as a function of the spatial frequency on a Nyquist sampling scale. This curve can be compared with an analytically calculated threshold curve for a given signal-to-noise ratio, shown in Figure S1 with a dashed red line. The point at which the threshold curve intersects the FSC curve determines the

spatial resolution, which in this case is 0.72 spatial frequency / Nyquist limit and corresponds to 19.9 nm. We note that this resolution estimation could be pessimistic because the correlation is computed from tomograms with only half of the projections in each. The coarser angular sampling can reduce the FSC at high spatial frequencies and provide a low estimate of the resolution, and as seen on figure S1 the line scan yields a slightly better spatial resolution of 18.9 nm.

S.2. Partial volume simulations

A)

C) Power function with Gaussian Cut-off (GC)

$$f(x) = p_1 \cdot (x - p_3)^{p_2} \cdot \begin{cases} \frac{\text{Gauss}(x, p_5, p_4)}{\text{Gauss}(p_5, p_5, p_4)} & \text{if } x \leq p_5 \\ 1 & \text{if } p_5 < x < p_6 \\ \frac{\text{Gauss}(x, p_6, p_4)}{\text{Gauss}(p_6, p_6, p_4)} & \text{if } x \geq p_6 \end{cases}$$

With $\quad \text{Gauss}(x, \mu, \sigma) = \exp\left(\frac{-(x-\mu)^2}{2\sigma^2}\right) \quad \begin{array}{|c|} \chi^2_{red} \\ \hline 1.06 \end{array}$

B)

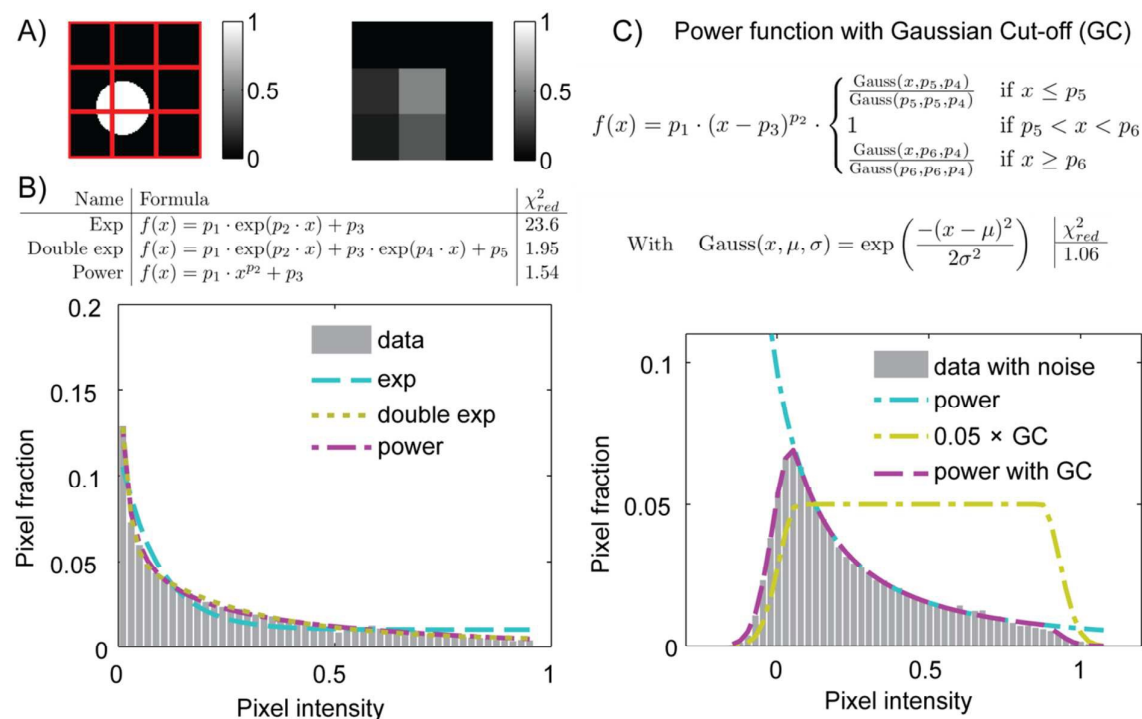| Name	Formula	χ^2_{red}
Exp	$f(x) = p_1 \cdot \exp(p_2 \cdot x) + p_3$	23.6
Double exp	$f(x) = p_1 \cdot \exp(p_2 \cdot x) + p_3 \cdot \exp(p_4 \cdot x) + p_5$	1.95
Power	$f(x) = p_1 \cdot x^{p_2} + p_3$	1.54

Figure S2: A) Illustration of simulation where sub-resolution cylinders (white =1, radius of 0.6 pixels) are randomly placed within a different medium (black = 0). The observed intensities due to partial volume effects are evaluated for 10^4 cylinders exemplified in the right figure. B) Resulting intensity histograms from the simulations described in A) are fitted with different functions. The goodness of fit is evaluated by reduced chi square assuming Poisson statistics and the power function is found to best match the distribution. C) The simulations are expanded to include Gaussian noise on the pixel intensities (σ = 0.05). To fit the new distribution the power function is multiplied with a step function with Gaussian Cut-offs (GC). The resulting fit yields a reduced χ^2 of about 1, and is shown along with two components of the fit: the power law function and the GC.

In a simulation carried out to calibrate the fit functions, a cylinder with diameter below the resolution was placed in a different medium, and the resulting partial volumes were calculated as shown in figure S2. 10^4 cylinders (r = 0.6 px) were randomly placed within the center pixel as illustrated in figure S2A using a uniform probability distribution without loss of generality due to the system symmetry. The resulting intensity distribution was fitted with different mathematical fit functions and found to be best described by a power law as shown in figure S2B. In real data sets the voxels will have noise due to experimental uncertainties, which is included in the simulation

as Gaussian perturbations of the pixel intensities ($\mu = 0$, $\sigma = 0.05$). The new resulting distribution of the simulated

noisy data is fitted with a product of a power function and a step function with Gaussian Cut-off (GC) as shown in

figure S2C. The function is evaluated to be a good description of partial volumes effects like sub-resolution

features based on the reduced χ^2 value near unity.
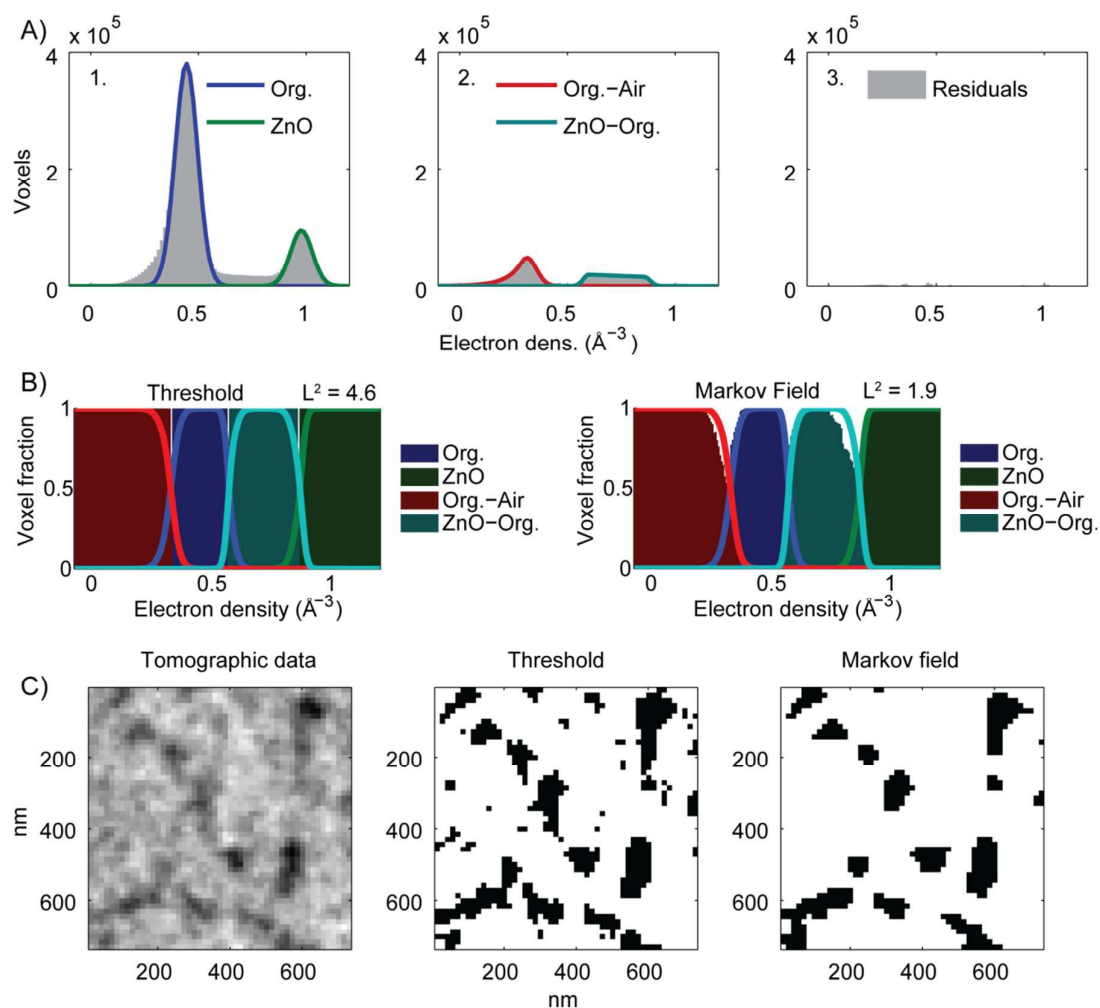
S.3 Markov field segmentation

Figure S3: A) Electron density histograms from a subset of the tomogram are fitted with (1) Gaussian functions for pure materials and (2) power functions with Gaussian cut-offs for material mixtures as described in S2, after subtracting the Gaussian fits in (1) from the histogram. With insignificant residuals (3) the data are described solely by these 4 functions carrying strict physical meaning. B) The fitted functions from A) are converted to relative amount of voxels for each electron density. These functions are compared to the actual fraction of voxel being segmented into the given label at the given electron density. The lines represent the fits in A) and the colored areas the actual segmentation in the tomogram. Measured by the L^2 norm the distance of Markov fields segmentation in only 40% the distance of threshold segmentation, Markov fields segmentation thus getting closer to true physical functions in A). C) Organic material (Landfester particles) with volumes containing air. The tomographic data is illustrated to the left and the two types of segmentation are shown to the right. Note

the Markov field is implemented in 3D and uses all neighbors, therefore also taking voxels out of the shown plane into account. The Markov field greatly reduces the noise present in the threshold segmentation.

The nearest neighbors were included in the segmentation by an α-expanded Markov field since it improves the segmentation and thereby more easily justifies the physical interpretations as illustrated in figure S3. The energy function that the Markov function minimizes is

$$E(f) = -\sum_{i \in C_1} \alpha_i f_i - \sum_{(i,j) \in C_2} \beta_{ij}\, f_i f_j$$

Here C_x is the x-clique, f is the segmentation label, and α and β are weights for the 1- and 2- cliques, respectively. In practice the α parameters were set to 1, and the β parameters were optimized by performing full segmentation combined with a pattern search algorithm to minimize the distance to the describing functions presented for a sub section of the tomogram in figure S3. In this example the functions give: Org.-Air(0.35 Å^{-3}) ~ $3.4 \cdot 10^4$ voxels and Org.(0.35 Å^{-3}) ~ $7.5 \cdot 10^4$ voxels, so the expected voxel fraction at 0.35 Å^{-3} electron density is ~0.3 for Org.-Air and ~0.7 for Org. material. The threshold segmentation gives Org.-Air(0.35 Å^{-3}) = 0 voxels and Org.(0.35 Å^{-3}) = $1.09 \cdot 10^5$ voxels thus reaching voxel fraction of 0 for Org.-Air and 1 for Org. material and residuals of 0.3 compared to their respective functions. The actual Markov segmentation was performed using a graph cut algorithm based on [Y. Boykov and V. Kolmogorov, *IEEE Trans. Pattern Anal. Mach. Intell.*, 2004, **26**, 1124–37].

S.4. Materials, fabrication, and photovoltaic characterization of tandem solar cells

Materials: Flextrode substrate that is comprised of Ag-grids/PEDOT:PSS/ZnO on PET substrate produced in a roll-to-roll machinery using Flexographic printing (Ag grids), rotary screen printing (PEDOT:PSS) and slot-die coating (ZnO)1,2 was acquired from InfinityPV (www.infinitypv.com). ZnO nanoparticle solution was also obtained from infinityPV in acetone with a concentration of 56 mg ml-1. P3MHOCT and PDTSBT-F:PCBM were synthesized in house.3,4 [60]PCBM with 99% purity was obtained from Merck. All organic solvents were of technical grade and purchased from Sigma-Aldrich with 99% purity. PEDOT:PSS Clevious P VP AL 4083 and PEDOT:PSS Clevious F010 were purchased from Heraeus Materials GmbH. Thermally curable Ag paste (PV 410) for the top silver electrode was purchased from DuPont. Sodium Dodecyl Sulfate (SDS) was purchased from Sigma Aldrich.

Fabrication: P3MHOCT and PCBM were mixed in a ratio of 1:1 in chloroform and processed into nanoparticles using the Landfester method[5] with Sodium Dodecyl Sulfate (SDS) as surfactant. The ink concentration was increased to 60 mg/mL by centrifugation. PDTSBT-F:PCBM was mixed in 1:1.5 ratio by weight and dissolved in chloroform with a solid concentration of 35 mg mL^{-1} . The mixture was heated on a hot plate at 70°C for 2-3 hours to achieve complete dissolution prior to the fabrication of the solar cells. Solar cells with inverted geometry were coated on Flextrode substrate. 1 m of these substrates were cut from the roll of Flextrode and subsequent device stacks were fabricated using a laboratory roll-coater.[6] Firstly, the P3MHOCT nanoparticle active ink was slot-die coated at a speed of 1.30 m min^{-1} and a flow-rate of 0.220 ml min^{-1} and a substrate temperature of 100 ^{o}C thus resulting in a wet-layer thickness of 17 μm and an estimated dry layer thickness of ~920 nm. On top of this layer, the recombination layer was printed through slot-die coating. The recombination layer comprised three layers.[7,8] Briefly, the first layer is a PEDOT:PSS layer based on Clevios F-010 diluted with isopropanol (IPA) in 1:4 *vol/vol* which is used as a wetting-agent/compatibilizer. This layer was slot-die coated at a speed of 1.30 m min^{-1} and flow rate of 0.10 ml min^{-1}. The second PEDOT:PSS layer consists of Clevios P VP AL 4083 diluted with IPA in 1:1 *v/v* which was slot-die coated on top of the compatibilizer layer at the same speed and a flow rate of 0.30 mL min$^{-1.}$

Finally, the recombination layer was completed by slot-die coating ZnO at a speed of 2 m min^{-1} and a flow-rate of 0.08 mL min^{-1} resulting in a dry layer thickness of 40 nm. All three layers in the recombination layer were coated at 60 ^{o}C.

On top of the recombination layer, the second active layer based on PDTSBT-F:PCBM was slot-die coated at a speed of 1.30 m min^{-1} and 0.120 mL min^{-1} at 60 ^{o}C resulting in a wet layer thickness of 9 µm and a dry layer thickness of 247 nm. The PEDOT:PSS back electrode was fabricated in a three step coating procedure as described elsewhere.[8] Finally, the Ag grid was flexo printed. All devices were annealed at 110 ^{o}C for 5 minutes post fabrication to achieve curing of flexo printed Ag grid while also annealing the photoactive layer. Individual cells were cut from the each stripe, and randomly characterized for photovoltaic properties. The device area was ~1 cm^2.

Photovoltaic Characterization

IV-characteristics were measured under 1000 W m^{-2} AM 1.5G condition using a Keithley 2400 source meter and illumination was provided by a KHS SolarConstant 575 solar simulator (Steuernagel Lichtteknik) which was calibrated with a reference photodiode to 100 mW cm^{-2} AM1.5G. Mismatch factors were not taken into account.

Table S1. Device photovoltaic performance with double sided illumination[1] is shown for the investigated tandem cells. All devices correspond to those reported in Table 1. BHJ$_1$ = PDTSBT-F:PCBM, BHJ$_3$ = P3MHOCT:PCBM and NP$_3$ = P3MHOCT:PCBM as Landfester particles.

	V_{oc}	J_{sc}	FF	PCE
	(V)	(mA cm^{-2})	(%)	(%)
Tandem BHJ$_1$ – NP$_3$	0.34	1.16	27.15	0.11
Tandem BHJ$_1$ – NP$_3$+ PCBM	0.60	0.68	29.18	0.07
Tandem BHJ$_1$ – NP$_3$+ BHJ$_3$	1.02	0.17	25.35	0.04

1. D. Angmo, S. A. Gevorgyan, T. T. Larsen-Olsen, R. R. Søndergaard, M. Hösel, R. Gupta, G. U. Kulkarni, F. C. Krebs, Organic Electronics, 2013, 14(3), 984-994.
2. M. Hösel, R. R. Søndergaard, M. Jørgensen, F. C. Krebs, Energy Technology, 2013, 1, 102-107.

3. J. E. Carlé , M. Helgesen , M. V. Madsen , E. Bundgaard , F. C. Krebs , J. Mater. Chem. C 2014 , 2 , 1290 .

4. M. Bjerring, J. S. Nielsen, A. Siu, N. C. Nielsen, F.C. Krebs. Solar Energy Materials and Solar Cells 92.7 (2008): 772-784.

5. T. Kietzke, D. Neher, M. Kumke, R. Montenegro, K. Landfester, and U. Scherf, Macromolecules, 2004, 37, 4882–4890.

6. H. F. Dam, F.C. Krebs, Sol. Energy Mater. Sol. Cells, 2012, 97, 191-196.

7. T. R. Andersen, H. F. Dam, B. Andreasen, M. Hösel, M. V. Madsen, S. A. Gevorgyan, R. R. Søndergaard, M. Jørgensen, and F. C. Krebs, Sol. Energy Mater. Sol. Cells, 2014, 120, 735–743.

8. D. Angmo, H. F. Dam, T. R. Andersen, N. K. Zawacka, M. V. Madsen, J. Stubager, F. Livi, R. Gupta, M. Helgesen, J. E. Carlé, Energy Technology. 2014, 2(7), 651-659

Nanoscale Accepted Manuscript